Hubble Space Telescope Imaging of HD 44179, "The Red Rectangle" [1]

Martin Cohen

Radio Astronomy Laboratory, 601 Campbell Hall, University of California, Berkeley, California 94720
Electronic Mail: mcohen@astro.berkeley.edu

Hans Van Winckel

Instituut voor Sterrenkunde, K.U.Leuven, Celestijnenlaan 200B, 3000 Leuven, Belgium
Electronic Mail: Hans.VanWinckel@ster.kuleuven.ac.be

Howard E. Bond

Space Telescope Science Institute, 3700 San Martin Drive, Baltimore, MD 21218
Electronic Mail: bond@stsci.edu

T. R. Gull

Goddard Space Flight Center, Code 681, Greenbelt, MD 20771
Electronic Mail: gull@sea.gsfc.nasa.gov

ABSTRACT

We present *Hubble Space Telescope* WFPC2 and deep ground-based images of "The Red Rectangle" (RR), a bipolar proto-planetary nebula associated with the post-AGB binary system HD 44179. The high-resolution *HST* images reveal complex new structures, many of them unique to this object. The RR nebula is dominated by a discontinuous "bicone", whose bright, sharp linear edges give the nebula an overall X-shaped appearance. The edges of the bicone are connected by a remarkable series of linear features elongated perpendicular to the radius vector, giving the object a ladder-like structure. The "rungs" of the ladder structure show a quasi-periodic spacing, suggesting that they have arisen from discrete episodes of mass loss from the central star, separated by a few hundred years. The total timescale over which mass has been shed into the visible nebula is of order 14,000 years. Outside the X-shaped bicone, parabolas curl inward, resembling wineglasses, that terminate on the bicone edges in large, limb-brightened vortices. The central object is bisected by a dark band, indicating that the star is not seen directly but is instead obscured by a surrounding opaque dust disk.

Subject headings: stars: individual — binaries: spectroscopic — stars: mass-loss — circumstellar matter — ISM: lines and bands

1. Introduction

The bright infrared (IR) source, RAFGL 915, was discovered in the rocket-borne IR Sky Survey by Price & Walker (1976), and identified by Cohen et al. (1975) with a peculiar nebula, "The Red Rectangle" (RR), associated with the star HD 44179. The term was coined by M. Cohen and K. M. Merrill during 1973 observations of the 8–13 μm spectrum of the object because of the distinctive appearance of HD 44179 on the Palomar Sky Survey as a rectangular object on the red plate yet an amorphous nebulosity, centered on a star, on the blue plate. Photographic images of the RR in 1975 showed a "biconical" nebula extending away from the central object. In a *Hubble Space Telescope* (*HST*) imaging program devoted to the central stars of planetary and proto-planetary nebulae, Bond et al. (1997) obtained short exposures in V and I of the RR in 1995. These WFPC2 images showed that the central star is not seen directly, but is obscured by a dark band which makes the object appear as two bright, osculating hyperbolic arcs arising from dust scattering of light from the star. This bisected structure had been partially resolved visually by early observers (Aitken 1918; Holden 1975; Heintz 1980) but interpreted as a close, resolved stellar visual binary. Speckle inferferometry by Meaburn et al. (1983) also partially revealed this structure, and was likewise interpreted as indicating a resolved binary. Also in ground-based high-resolution data, the central object was found to be resolved (Roddier et al. 1995; Osterbart et al. 1997). Thus, the RR represents a canonical example of a bipolar nebula whose illuminating source is visually obscured by an almost edge-on, dense, dusty disk.

Indeed, the RR has become the archetype of a succession of bipolar nebulae (BPNe), primarily recognized because of their very large ratios of IR to optical brightness and generally regarded as reflection nebulae. However, the RR is unique in several respects, most notably in the structure of its nebula which consitutes the primary focus of this paper. No other BPN harbors the remarkable biconical appearance of the RR, nor the plethora of still unidentified molecular bands in emission on top of the characteristically broad "extended red emission" (ERE) (Cohen et al. 1975; Witt & Boroson 1990) which is so intense and arises in situ in this nebula (Schmidt et al. 1980; Scarrott et al. 1992; Sarre et al. 1995; Van Winckel et al. 2002). The central source of the RR is an A-type post-asymptotic-giant-branch (post-AGB) star, which has been found to be a single-lined spectroscopic binary (Van Winckel et al. 1995). The updated orbital period is 319 ± 3 days, the eccentricity is a remarkably high $e = 0.37$, and f(M) = 0.52 $M_\odot$.

In a new series of papers we explore the RR in unprecedented spatial and spectral detail. Van Winckel et al. (2002) identify many more unidentified, optical, molecular bands than previously known in the RR's spectrum on the basis of previously unpublished, ground-based, high spectral resolution material. The present paper examines the structure of the RR, combining deep ground-based exposures of the outermost nebula with WFPC2 images of the inner nebula from both PC and WF cameras of the *HST*. We use these images to investigate the symmetry, frequency, and

---

[1] Based on observations with the NASA/ESA *Hubble Space Telescope*, obtained at the Space Telescope Science Institute, which is operated by AURA, Inc., under NASA contract NAS5-26555

density of mass-loss in the two lobes of the RR, and to infer the processes through which the apparent bicone was formed, by our interpretation of previously unknown morphologies in the RR.

In §2 we describe the observational material and present the results of unsharp masking of these images; in §3 we separate the structure into its newly revealed components; in §4 we measure the angular separations of the separate mass-loss events from the central source. §5 seeks parallels with other astronomical objects associated with nebulae of similar relevant structure and explores to what extent the binary nature of HD 44179 may be responsible for the startling geometry of the RR.

2. Observations and data reduction

2.1. Exposures

Tables 1 and 2 detail our observations. The deep ground-based exposures were obtained on the ESO 3.5m NTT telescope at La Silla with the multi-mode instrument EMMI. The scale on the TEK 2048x2047 CCD was $0.268''$/pix. A coronograph was simulated by inserting a transparant plate with 6 black dots of different sizes in the starplate wheel. No optical component reduces the scattered light, so in the very bright center of the RR close to the coronographic mask, the images are corrupted by scattered light from the black dots. For the Hα image we have put the RR center behind the $1.9''$ dot, while for the other filters we used the $4.8''$ dot. Seeing varied between 1.2–$1.5''$ during the observations.

WFPC2 observations were secured on 1999 Mar 17-18 in a series of short and long exposures, with all the longer exposures split into two, for cosmic ray elimination. To probe the scattered starlight we chose the F467W filter. To include the strongest of the groups of molecular bands in the RR we selected F588N (for the 5800Å complex), F631N (near the peak of the ERE but matched to the 6380Å band), and F622W to match the bulk of the broad ERE peak. In reality, as we found from our STIS spectra (Gull et al. 2003), each of these red filters is largely dominated by the ERE. All four filters were applied to the inner nebular structure by placing the RR near the center of the PC1 chip with its $0.046''$/pix. We later rotated and repointed *HST* to place the center of the RR in WF3 with the rest of the biconical nebula crossing into WF2, all with $0.1''$/pix spatial resolution. These images cover a greater extent of the RR because the WF pixels are coarser than those of the PC chip and each cosmic-ray-split exposure was 500s long. Note that our ground-based images go still farther out into the nebula due to their long exposure and the increased light-grasp of the NTT telescope.

2.2. Image reduction and processing

Standard reduction of the ground-based images inluded bias correction, flat-fielding and cosmic hit cleaning and was performed in the MIDAS environment. We did not attempt to flux calibrate the images because the space-borne *HST* images are much better calibrated.

Starting from WFPC2 standard pipeline products (i.e. bias-corrected, flatfielded, flux calibrated images), we eliminated cosmic rays by comparison of all CRSPLIT images. This was done for both the PC and WF images separately. For the F588N and F631N WF images we made mosaics of the WF2+WF3 frames.

The purpose in securing PC short exposures was to be able to insert correctly-scaled versions of these into the PC long exposures, whose central portions were all saturated. For F467M we had no corresponding short exposure so we inserted a scaled F502N image into the combination of the two 260s F467M images. All such insertions were carried out by careful registration of the scaled images. The scale factors we applied to the short exposures to substitute them into the longer exposures were: 88.3 (F502N into F467M); 22.46 (F588N); 12.09 (F631N); 57.14 (F622W). We derived the latter three factors simply by the ratio of long to short exposures, multiplied by the ratios of PC gains in the appropriate gain mode. To place F502N into F467W, we estimated the scale as the product of exposures, gains, and approximate FWHM bandwidths, leading to 94.9, but experiment indicated 88.3 to be a better match.

These reductions led to four complete, unsaturated, independent PC frames in F467M (with F502N), F588N, F631N, and F622W, and two additional WF image mosaics in the F588N and F631N filters. We explored methods to correct for the strongly diffracting spider by deconvolution with the PSF but neither the artificial PSFs produced by Tiny Tim, nor PSFs deduced from single bright star measurements from the archive, were defined far enough from the center to correct for the strongly saturated and resolved central image. We, therefore, decided not to compensate for the diffraction from the spider.

2.3. Direct images

Figure 1 offers our Hα ESO NTT image, in which we replaced the center by the correctly scaled and rotated F588N WF image. Note that the nebula is much bigger than generally acknowledged. We discover emission up to 56$''$ from the central source and along a spike of the clear X-shaped nebula. The total extent of the nebula is some 2$'$ on the sky ! The faint arc which is seen on the symmetry axis in the northern part of the nebula (Van Winckel et al. 2002) is detected only in our Hα filter and not in the deeper continuum ERE filter image (not displayed here). We interpret this as due to very weak Hα emission in the northern pole of the disk. The arc has a diameter of about 12.5$''$ and is only observed in the northern pole where the top of the arc is at 38$''$ from the central source.

Figures 2 and 3 offer a good representation of the wavelength dependence of the observed structure and morphology of the RR in our PC images. The blue exposure is striking because of the complete absence of *any* X-shaped nebulosity around HD 44179. The RR center is clearly resolved and the dark optically-thick central dust lane is visible, along with the bright polar regions of scattered light. The extended nebula is rather circular in this filter. The "Red Rectangle" is better characterized as a "blue circle", if only the scattered light outside the ERE is observed. The contrast with the F622W-filter image (Fig. 2, right panel) is striking. This image clearly shows the complex structure of the ERE emitting material, which has a low scattering efficiency. This indicates a chemical/physical difference between the compact central region and the extended, presumably younger, X-shaped nebula. In the sharpened blue PC image (Fig. 3), three concentric nebular arcs are visible. A detailed comparison with PSF models shows, however, that these are not real, but are but PSF-related Airy rings.

The F622W exposure is our deepest single PC image due to its large bandwidth but, because of the dominance of the ERE, the F588N and F631N images contain virtually identical information, albeit with somewhat higher noise. In the F622W image (Fig. 2, right panel) the complexity of the inner nebula is apparent and, in what follows, we discuss the different features in more detail. The center of the nebula in the F467M and F662W images is very bright and both compound images span a dynamic range of 10^5. This is illustrated in Fig. 4, where we plot traces along the images. We defined one trace along the dark dust lane, and one perpendicular to it, along the polar symmetry axis of the nebula. In the blue, the two flux distributions are very similar, except for the very center of the nebula; in the red, the difference is very clear and the different local flux peaks are apparent even in the logarithmic profile. The blue scattered light is well represented by a power law with spatial index -2.7 (Fig. 5). This suggests that the radial density profile of scattering particles is not too different from a simple r^{-2} law, assuming an optically-thin nebula.

2.4. Three-color images

We used the Interactive Data Language (IDL) to produce a three-color combination image of the RR using F467M (blue), F588N (green), and F631N (red) and, in another combination, substituting F588N, F622W, and F631N for the blue-green-red triad, respectively. In order to overcome the high dynamic range, we transferred the files in a logarithmic form and byte-scaled in a 0-255 range before combining in a RGB format. Figure 6 illustrates strikingly how the central portions of the RR, very close to HD 44179, are characterized by scattered stellar continuum (blue), while the nebula itself remains essentially uniformly yellow (equal contributions from F588N and F631N). By contrast, the F588N, F622W and F631N combination is notable for the almost complete absence of color anywhere. The structure of the RR is basically a map of the distribution of the ERE and there are very few, if any, regions in which the sharper molecular complexes contribute differentially to this white image.

The related product from the WF material (not shown) returned the same results with virtually the entire nebula in a uniform color, except along the stellar diffraction spikes (which, of course, have a different wavelength dependence because of diffraction effects). To summarize these results, there can be few if any locations in the RR nebula in which the groups of sharp molecular bands behave differently from one another, or dominate the broad ERE.

The innermost portion of the RR as defined by the PC is noteworthy. One clearly sees that "HD 44179" is a pair of hyperbolic curves, almost in contact, with the southern element brighter than the northern. These correspond to the inner envelope that scatters the starlight. Equally notable is the large opening angle defined by the limit of the hyperbolic arcs defined in our data, whereas the rest of the RR's structure is constrained to lie in a much narrower bicone.

2.5. Unsharp masking

The extremely high dynamic range in our images, where we have substituted short exposure images into long, makes it difficult to display images of the RR with the full panoply of detail from HD 44179 far out in the nebula. We experimented with unsharp masking as a way to enhance the inherent structure of the RR from close to the star to far out in the nebula. Using IDL we coded several different algorithms. These varied from the simple division of an initial image by a Gaussian-smoothed version of the same image (as in IRAF), to that implemented in MIDAS, where the difference image, between the original and Gaussian-smoothed versions, is scaled, lightly smoothed (with a 1×1 pixel Gaussian kernel), and then added back to the first Gaussian-smoothed image. We also worked with a subtractive technique, removing a Gaussian-smoothed version from the original image. For greatest utility and ease of display we settled on the MIDAS variant.

Because we found imperceptibly few structural differences between the two WF mosaics, and between the three (non-blue) PC filter images, we created combined images of these to increase signal-to-noise. These combinations were based upon inverse-variance weighting of the separate images, according to the noise measured in regions of the images far from the RR's nebulosity.

We investigated the merits of different smoothing kernels, from 1×1 up to 21×21. Different kernels accentuate different spatial structures so we examined closely the 5×5, 9×9 and 21×21 smoothing. We applied the kernels to three-filter PC-combined images and to the similar WF product. It is apparent that smoothing kernels larger than 3-5 pixels are essential to avoid granularity, but the largest kernels lead to unacceptable loss of information close to the center of the nebula. We settled on unsharp masking by a 9×9 pixel region.

Figures 8 and 9 present the 9×9 pixel masked versions of the rotated three-filter PC-combined image, and the two-filter WF-combined image. The rotations were applied to compare ground-based, WF, and PC image structures, and for the express purpose of taking the same vertical slice through the inner structure of the RR in each image.

3. The nebular structure

The overall structure of the RR is contaminated by a pair of prominent diffraction spikes. These artifacts run from the top right corner to the bottom left corner of Figure 8 (roughly cutting the RR's long axis of symmetry at 45°), and orthogonal to this. This latter spike unfortunately runs along one of the edges of the bicone although one can separate it with care, by eye. The RR is dominated by the "X" structure (i.e. the bicone), which has been known since the mid-1970s, and this is *not* an artifact. But the new WFPC2 images, particularly in their unsharp-masked variants, give us a totally new perspective on the RR.

There are three fundamental structures never before recognized within the RR. For convenience, we term these the "ladder" (whose rungs link the the edges of the bicone and are roughly parallel to the plane of the inferred edge-on circumstellar disk that hides the central star); the "wineglasses" (whose projected edges embrace the bicone but curve around and terminate on the bicone); and the "vortices", which represent substructure simultaneously coincident with the rim of each wineglass, the attachments of each ladder rung, and the bright segments of the bicone, which is itself probably discontinuous, being defined solely by the confluences of these other bright features. *None of these new morphologies is an artifact.*

3.1. The "ladder"

The ladder is most startlingly revealed in the unsharp-masked PC and WF image (Figures 8 and 9). A series of nebulous strands, generally parallel to one another, connects from one bicone edge to the other, and is also seen in the inner (PC) and outer (ground-based) image structure. On closer inspection, however, one readily sees that some of these strands do not span the full width of the bicone; fragmentary pieces are well shown in the southern RR in Figure 8. Others are not parallel to the neighboring rungsare and are inclined, rather than perpendicular, to the bicone's long axis of symmetry. More remarkable yet is the trio of "figure-eight" filaments evident in the innermost PC structure (Figures 6, 7): a bright one , immediately N of HD 44179 and a pair to the S, the brighter one symmetrically disposed with respect to that in the N, the second, fainter one, lying just S of the brighter.

We have found it fruitful to interpret the multiple facets of nebular morphology in terms of distinct episodes of mass loss from the central star. In what follows we implicitly make this assumption. Other authors have argued alternatively that quasi-periodic structures seen in other bipolar protoplanetary nebulae (such as periodic circular arcs) may be due to an instability in the outflow rather than to episodic mass loss from the star (Simis et al. 2001).

We have the strong impression that the distinct episodes of mass loss that have produced the strands have generated more chaotic structures most recently, i.e. in the innermost parts of the nebula, while the earlier (more distant) events have led to a much more regular ladder of nebulous strands. Indeed, it seems possible to visualize the organization of *all* strands across the nebula sampled by the PC as a set of figure-8s, rather than as a jumble of a few complete figure-8 loops and many separate nebular fragments, some of which do not attach to both of the bicone edges, while others exist only as tiny portions of a strand. However, in such a picture, the degree of disorganization is greatest well within the PC nebulosity, and least far out in the WF structure. This could be either a matter of diminishing detectability of fragmentary strands with distance from the star due to faintness, or a physical phenomenon.

The separation between adjacent strands (or figure-8 loops) clearly increases with distance from the central object. If interpreted as episodic mass-loss events, these events were more frequent recently than in the past, or the mass-loss is accelerating.

3.2. The “wineglasses”

These refer to the spectacular sequence of parabolic arcs, visible N and S of the center of the RR, that dominates the structure of the nebula, perhaps most readily seen in Figure 8, but evident in direct images (e.g., Figures 2 and 7) as well as in the WF and ground-based material. The innermost arcs are most evident and most complete, and strongly resemble wineglasses (inverted in the S lobe) filled to their brims, with limb-brightened gaseous surfaces represented by the strands described above. Previous analyses of the RR have indicated the need to invoke *hollow* biconical surfaces rather than conical volumes so one must be cautious with such analogies.

The arcs constitute a nested sequence, with the innermost parabolas the smallest and brightest, and the outer arcs, of widening opening angle, containing all the inner. This sequence continues out into the WF images, well-shown again in the unsharp-masked data (Figure 9, right panel) but, in this region, the most striking elements are the edges of the parabolas furthest from the star where brilliant knots appear (Figure 8). Further still from the star (Figure 1, central insert) one has the impression that there may be no truly continuous “biconical” surface; there is only the envelope of these bright knots, which also mark the boundaries of each rung. The S parabolas are brighter than those in the N lobe, consistent with the view that the RR is tipped with the S lobe toward us, and the N tilted away, which we also confirm from our ground-based and STIS spectroscopy.

3.3. The “vortices”

Detailed scrutiny of the SW RR spike (Figure 8) reveals these bright blobs to be resolved vortices, wrapping inward toward the long axis of symmetry of the RR. No fewer than three adjacent vortices can be seen whose (dark) centers contrast sharply with the surrounding nebulosity of this spike, as opposed to appearing solely as undifferentiated bright knots. In Figure 8, the white arrows indicate several of these bright terminations of the arcs and resolved vortices. Similar vortices, albeit much fainter, appear along the NW spike too. The ground-based deep images enable one to follow the series of vortices much further from the star than the WF images, but the pattern is unchanged. Each bicone edge (or spike) is delineated by a series of brightenings associated with a matching pair of vortices and a strand that crosses the bicone to link these vortices. The vortices are evident even in the earliest of our deep photographic images taken by one of us (TRG) with the KPNO 4-m telescope (Cohen et al. 1975: their Figure 1c), as the terminations of each of the edges of the extended bicone. The previously inexplicable angles at which those terminal nebulosities lie on the continuation of the spikes is now understandable as the combination of pairs of bright vortices with the associated strongly curved ends of the parabolic arcs that impart the non-collinear character of these faintest nebular regions.

3.4. The innermost nebula

To investigate the ERE emission itself close to the bright central region which is dominated by the scattered light from the central stars, we regridded the PC 467M and PC 622W filter images to a finer grid of 0.1 original pixels and carefully aligned and scaled the two images before subtraction. The excess emission of the ERE on top of the much stronger scattered light is clearly observed in the poles of the obscuring disk (Figure 3). The opening angle of the ERE emission at $0.3''$ of the central stars is only 40°, this in contrast to the much wider opening angle of the extended nebula where the angle of the outer cone in Fig. 1 is 80 degrees. Also in Fig. 6 and Fig. 7 the gradual widening of the opening angle of the cone is visible.

4. Mass loss from HD 44179

To assess the character of HD 44179's mass-loss and to examine the episodic events that have sculpted the RR's structure, we used spatial slices through identically unsharp-masked versions of the ground-based coronographic Hα, the two-filter combined WF, and three-filter combined PC images. The registration of the WF and PC profiles was checked by establishing the zero point of each according to the central peak, i.e. the brighter (southern) vertex of the inner scattering nebula. Two schemes were implemented. In the first, all columns within the central region of the bicone were coadded; in the second, the maximum number of columns possible was coadded, consistent with avoiding stars projected toward the RR but staying within the outermost confines of the bicone. The two approaches resulted in very similar results, but we favored the second method because of its robustness (some strands do not cross the center of the bicone) and the greater signal-to-noise of the resulting coadded profile.

Fig. 10 compares the spatial profiles through the PC and WF images in the inner nebula where the combined PC data still have adequate signal-to-noise to define the ladder. One clearly sees the difference in pixel size between the PC and WF chips (roughly a factor of 2.2) in this figure, although the agreement within $7.3''$ of the center of the RR is highly satisfactory. The right panel similarly compares spatial slices through the ESO Hα and the same WF image, but now in the intermediate range within $\sim$15$''$ of the center of the RR. Again the agreement is adequate, bearing in the mind the much coarser resolution of the ground-based data, limited by $\sim 1''$ seeing. There are some striking differences between PC and WF slices, most notably the fact that the WF detects a rather broad (FWHM 0.47$''$) band of nebulosity centered 3.76$''$ N of the star, while the PC resolves this into a pair of narrower features (FWHM $\sim$ 0.3$''$) at 3.47$''$ and 4.05$''$ N of the star, that flank the WF's spatial profile. This is not simply an issue of differing resolutions of the two cameras. In fact, it arises because the spatial coadd of many columns in the WF image does not resolve this strand into its true figure-eight character whereas the PC coadd detects two narrow features corresponding to the upper and lower edges of the horizontal "8"s.

Table 4 concatenates the information from these three independent spatial slices summarizing, for N and S lobes of the RR, the centroids of the strands of nebulosity that constitute the rungs of the ladder. If we identify each strand as a separate event, either N or S, we can identify a certain amount of N-S symmetry in the RR. But clearly the N has been more active than the S, with a greater number of episodes. The unsharp-masked pictures suggest that there is little or no mass loss between these events but it is the nature of the technique to emphasize structures by sharpening gradients in brightness. The innermost nebula is dominated by scattered starlight, as characterized by the bluish halo around the center of the RR in Fig. 6 and, out in the bicone, the direct images are overlaid by generally bright, diffuse ERE, so that it is difficult to estimate how dark the bicones really are, between the lattice of strands. However, there is typically a 10-25% change in surface brightness, in each of the WF and PC direct frames, crossing strands within the bicone, and typically a factor of two measured along the NE-SW spike crossing the vortices.

Of particular interest is the brightness distribution along the NE-SW spike, or bicone edge (along which our STIS observations were taken: these will be described in a forthcoming paper, Gull et al. (2003)). Because the parabolic arcs terminate along this spike in the vortices, we can avoid the complexities of the figure-8 nebular strands by examining a profile of stellar mass loss as mapped along the spike. We rotated our standard unsharp-masked (9×9) version of the combined-filter WF image 16° clockwise in order to take our vertical cut along this spike. Fig. 10 compares the WF and PC profiles along the spike, each assessed from relatively narrow slices to avoid contamination by the arcs and especially by the ladder.

While there is generally reasonable agreement between PC and WF spatial profiles, there are also places along the spike where PC peaks flank a WF peak, exactly as in the vertical slices coadded through the ladder (e.g. $\sim 4''$ NW). It is also noteworthy that these profiles contain features that are often much broader than profiles taken across the strands, as if the different mass loss events have tended to spread out and merge along the spike, whereas they appear to be more distinctly separated across the strands.

Do we see evidence for symmetry and periodicity within these apparently episodic mass loss events? Superficially there appears to be no N-S symmetry. But, although the S lobe of the RR clearly contains fewer individual, bright, *complete* strands than the N, it does have a greater number, if we include fainter and fragmentary strands. If we quantify the mean separation between distances of all strands, whether partial or complete, in three separate zones, roughly sampled by PC, WF, and our ground-based images we find the following. Within $6''$ of the star, $6 - 12''$, and $12 - 40''$, the N lobe gives $0.62''\pm0.09''$, $1.52''\pm0.31''$, and $2.80''\pm0.45''$, respectively. The S lobe treated identically gives $0.40''\pm0.09''$, $1.26''\pm0.16''$, and $2.64''\pm0.29''$, respectively. Statistically we find no significant differences between the lobes, though we note that these averages do depend on the assumption that strands are equally detectable in both lobes. However, there are clear indications that the mean spatial separation between strands steadily increases as we sample older and older mass loss events.

The evidence for spatial periodicity within the RR is greatly complicated by the figure-8 strands. If we simply treat each of these as having a central spatial location (essentially at the crossing point of the two loops in each figure-8) there is no N-S asymmetry, i.e. the disparity in number of figure-8 loops between N and S vanishes. The average separation from HD 44179 between the four centers of figure-8 loops in each lobe is: N, $1.46'' \pm 0.29''$; S, $1.21'' \pm 0.22''$. These are not significant differences, and might be construed as evidence of coarsely periodic bipolar mass loss.

To convert these separations into time scales for mass loss is not possible because we lack direct probes of the velocities across the entire RR. Were we to assume simply a constant outflow velocity within the bicone, of 7 km s^{-1} (Jura et al. 1997), at a distance of about 710 pc (Men'shchikov et al. 2002), then we would conclude that mass loss episodes are becoming more frequent, occurring roughly every 70 yr in the inner (PC) nebula, and 400 yr (WF) up to 2000 yr (as measured in the deepest ground-based images) in the outer. Of course, our simplistic assumption of constant velocity of mass loss ignores the possibility that more recent ejections encounter high ambient densities within the confines of the nebula due to the older outflows. The most distant events we can detect in our ground-based Hα image are about 40,000 AU (0.19 pc) from the center of the RR. Assuming a 7 km s^{-1} constant outflow velocity, the dynamical age of the nebula is thus about 14,000 years.

5. Discussion

5.1. The nebula

Many BPNe have emerged from infrared sky surveys, often with bizarre morphologies. Recent *HST* imaging surveys have revealed that the basic inner structure of many post-AGB stars consists of an optically-thick, dusty disk obscuring the direct view of the central star(s), and a BPN seen in reflected light (Sahai et al. 1998a, 1999,b,b; Ueta et al. 2000; Kwok et al. 2000). The best studied example is certainly the "Egg Nebula" (AFGL 2688) with a superficially similar inner morphology to that of the RR; namely, an optically-thick disk or cocoon, seen nearly edge-on, and starlight, escaping along the polar directions (Sahai et al. 1998a). In both nebulae the central star is of roughly comparable effective temperature. Both show a considerable amount of dust processing with indications of the presence of very large grains in their disks (Jura et al. 1997, 2000). The bipolar reflection nebula in AFGL 2688 is a pair of "searchlight" beams defined by scattered, highly-polarized, starlight but the RR nebula is dominated by nebular ERE emission.

Despite the similarities with the RR, the Egg Nebula lacks any hint of vortices, parabolic arcs, or a ladder-like structure. Further, other differences indicate that dissimilar physical and chemical processes are involved in the formation of nebulae around both these post-AGB objects. AFGL 2688 is well-known for the presence of numerous concentric arcs suggesting episodic, spherically symmmetric density enhancements in the 150-450 yr range. While the true nature of these is still a matter for debate (e.g. Simis et al. (2001); Soker (2002)), the morphology of AFGL 2688, in which complete spherical arcs are traced, argues for a process that occurred prior to the formation of the thick dusty torus seen in the high spatial resolution images of Sahai et al. (1998a). The inner structure of AFGL 2688 is very complex with point-symmetric morphology and collimated, bipolar, fast outflows with different orientations seen both in CO (Cox et al. 2000) and H_2 (Sahai et al. 1998b). The images presented in this paper show that, in the RR, the nebula itself is strongly constrained by the dusty central disk presumably formed prior to the formation of the nebula. This is consistent with the presence of O-rich dust in the disk, while the nebula itself is C-rich (Waters et al. 1998). On the other hand, the purely reflected light of the RR, sampled by the blue filter (Fig. 2, left panel), is remarkably spherically symmetric outside the innermost core.

The Egg Nebula is rather rich in molecules (e.g. Cernicharo et al. (2001)) and its complex inner kinematics are traced by interferometric CO microwave emission (Cox et al. 2000). By contrast, the RR is an extremely feeble CO emitter and its faint, narrow CO lines indicate a outflow velocity of only 7 km s^{-1} (Jura et al. 1997).

On purely theoretical grounds, Icke (1981) argued that biconical outflows are a natural consequence of flows above luminous disks and might be the underlying mechanism that shapes all BPNe. Of interest in Icke's paper is an illustration of a specific example of such a flow, which also shows parabolic isodensity contours (his Fig. 2). In recent detailed modeling based on the images that we discuss here, Icke (2002) represents very similar structures by a spherically symmmetric intermittent wind which is focused by an oblique shock and creates biconical structures. Finer details, such as the widening of the opening angle and the presence of presumably shocked Hα emission along the symmetry axis, are also predicted by his model. The vortices on the X-shaped spikes are not immediately apparent but the higher density knots on the X-shaped spikes could very well be strongly turbulent. The model discussed Icke (2002) uses an outflow velocity equivalent to Mach 35, which is rather high compared with the CO data, but there is evidence for high velocity gas somewhere in the system from UV data (Glinksi et al. 1997) and Hα (Jura et al. 1997). Our STIS data indicate the Hα emission to be visible only in the innermost nebula. Jura et al. (1997)

conclude that the fast gas is likely to be confined to a much smaller zone which fits within the binary's orbit. A detailed comparison with the models of Icke (2002) that addresses not only the morphology but all the physical data deduced from our images and the contraints from the SED modeling (Men'shchikov et al. 2002) will be necessary further to constrain the geometry of the inner region of the system.

The intermediate polar/cataclysmic variable object V603 Aql (Nova Aql 1918) offers us an another important paradigm for episodic mass loss within a binary system. Weaver (1974) has assembled the copious optical spectra taken in a variety of position angles on the sky from Lick Observatory during 1919, and has been able to reconstruct a physical three-dimensional model of the bipolar shell associated with this eruption. V603 Aql's shell was "composed of truncated coaxial cones" and the entire system is viewed from very close to the rotation axis of the binary. The nova ejecta collide with the disk which, in V603 Aql, surrounds only the prenova and not its companion. These collisions force matter to flow off the inner edge of the disk in "conically-shaped streams". Weaver speculated that this phenomenon, and its results, should characterize all novae. From the abundant slit spectra, Weaver deduced that cones of different opening angle were implicated in the bipolar shell surrounding V603 Aql, with the narrowest opening angles being associated with material most distant from star. One might speculate that the narrowest cones correspond to the fastest velocities and earliest ejecta, from a time when the circumstellar disk was densest, while the progressively more open cones are due to later events, by which times the disk had been significantly eroded radially, lessening the constraint on the geometry of mass loss.

What of the vortices? One might argue that if V603 Aql had shown these then the fortuitous matching of binary rotation axis with the line-of-sight to the sun would have made it extremely difficult to recognize such vortices, because they would be viewed through the set of truncated cones, rather than at the edges of the flow as in the RR. The vortices are such outstanding features of the RR's structure that they must have significance, particularly because they are such large structures in the RR. We have identified the edges of the bicone as the envelope of those locations where the vortices wrap around, and the strands as originating from the bright cores of these vortices. The widths of the strands, however, are smaller than the overall scale of the vortices and we have yet to account for the figure-8 loops.

If we argue that each episode of mass loss from HD 44179 encounters the circumbinary disk and is deflected by the disk then we must ask whether every episode is associated with both N and S flows, or merely with one or the other. If regularity were maintained then pairing of events seems much more likely than randomness, and we would argue that figure-8 loops are the primary consequences of such episodes. The strands would represent the limb-brightened envelopes of the upper surfaces of the gas flows. Presuming cylindrical symmetry, the vortices must occur around the entire rim of each paraboloidal ejection, representing the locus of greatest density as well as brightness (for optically-thin emission). Thus we would expect the parabolic arcs to exceed the size of the high density vortices, hence explaining the thickness of the gas surfaces viewed edge-on. If the ejecta could not maintain cylindrical symmetry, for example, due to irregularities in the density of the inner edge of the circumbinary disk, then parts of the paraboloidal envelope would be occupied by gas to greater distances than the rest.

The inner radius of the dust disk is not very well constrained because it depends on the chemical characteristics of the dust species which can condense/sublimate close to the central objects, but the orbit fills a significant fraction of the inner dust-free region. This implies that the mass-losing star in its highly eccentric orbit can never be truly centered in the dusty tunnel through which starlight passes and is scattered in our direction. Consequently, unlike V603 Aql, where the pre-eruption disk was associated only with a single star in the system, we would not expect material ejected spherically from HD 44179 to encounter the circumbinary disk at the same times in different directions. It is this inherent lack of centering that caused the fluid flow to have risen to different heights azimuthally on the paraboloids, giving rise to the figure-8 loops as we view those azimuthal variations almost edge-on.

If the perturbation of a single mass-loss event were to have a sinusoidal character due to rotational modulation, with two maxima and two minima per revolution in the height of the leading gas along the paraboloidal surface, then the limb-brightened leading edge of the gas along the hollow paraboloidal surface would appear as a figure-8 loop, with the relative sizes of the two loops depending on the aspect in which we view the event. Irregularities in flow density would also rather naturally account for the apparently detached fragments of some strands, rather than our observing complete, symmetric, and uniformly bright loops.

5.2. Evolution

Waelkens et al. (1996) have presented a geometric model for the circumbinary disk that relates it to the dimensions of the binary orbit. Unusual in the RR is the enormous scale height of the dusty disk, some two orders of magnitude larger than the binary orbit, and the significant current orbital eccentricity.

The most recent modeling of the peculiar SED comes from Men'shchikov et al. (2002) and is based on high spatial resolution ground-based speckle data coupled with the broadband SED. The basic geometry is a geometrically and optically-thick torus-like density distribution with bipolar conical cavities carved out by a faster wind. The SED modeling, together with estimates of the interstellar reddening, gives a distance of 710 ± 70 pc, which we use in this paper. The similar morphology of the inner nebula in the broad wavelength range from 0.6 to 10 μm implies very large scattering dust particles. The spikes were simulated in the 2D model by artificially increasing the scattering term in the cavities. As our blue images show, to model the spikes one has to take into account the ERE emission, because the purely scattering photons give a different geometry. Although the SED is very well fitted with this model, there remains a problem with the history of the nebula: the torus in the model is expanding with a crossing time of only about 100 years due to a very recent phase of heavy mass loss. Moreover, since part of the trapped dust is O-rich while the hotter inner dust is C-rich (Waters et al. 1998), this would imply a very recent chemical transformation. The extended nebula is clearly confined by the inner geometry. (Bujarrabal et al. 2003) have reported the discovery of a rather thin equatorial disk around HD 44179 that is very likely in Keplerian rotation, probably the first such disk to be observed around a post-AGB star.

Consequently, one of the main problems in understanding the RR remains the history of formation of the different structures, particularly the formation and stability of the inner dusty region, presumably prior to the creation of the nebula.

6. Conclusions

In this paper we present new, high spatial resolution optical images of the Red Rectangle nebula obtained with the WFPC2 camera onboard the *HST*, together with coarser but deeper ground-based coronographic images.

The RR is extremely well resolved and the inner and outer structure can be studied in great detail. The inner structure of the nebula, with an optically-thick dust layer blocking the direct view to the central object, and the optical light escaping into the polar lobes and scattered in our direction is rather common in the high spatial resolution images of post-AGB objects (Ueta et al. (2000) and references therein). The inner structure of the RR is also resolved in ground-based high spatial resolution data (e.g. Men'shchikov et al. (2002)) and shows the same morphology, even in near-IR images. In our blue image, sampling only scattered starlight, the nebular structure is clearly different, and it is the ERE that dominates in the BPN. This conclusion is echoed by new, diffraction-limited, mid-IR imaging and spectroscopy with the Subaru 8-m telescope by (Miyata et al. 2003), who show that the X-shaped morphology is already established within $3''$ of the central object. Further, this inner nebular structure is dominated by the emission of the 8.6 and 11.2 μm bands (often attributed to polycyclic aromatic hydrocarbons), rather than by scattered mid-IR continuum.

The *HST* images presented in this paper reveal a complex nebula consisting of a set of limb-brightened paraboloids in both polar directions. Other striking nebular characteristics are a set of vortices on the X-shaped limb-brightened edges of the nebula and, in between the X-shaped edges, a series of strands (the ladder). These are more complex and frequent in the inner nebular region, but clearly discrete and less frequent in the outer regions. The series indicates a distinct set of mass loss events, shaped by the inner, stable, dusty region surrounding the central stars. Using the most recent distance estimate (Men'shchikov et al. 2002) of 710 pc and an outflow velocity of 7 km s^{-1}, the dynamical timescale of the nebula is 14,000 years. The mass loss events occur in the range 100–700 years, too large to be linked to the orbital period ($\sim$ one year) but too small to be related to thermal pulses. The timescale of these episodes is very similar to that of the spherically symmetric arcs observed in several other post-AGB objects. In the RR, these mass loss events were clearly shaped by the stable inner dust disk which must be both older than the nebula and chemically different from it. This is consistent with the presence of O-rich material in the otherwise C-rich nebula (Waters et al. 1998). Recent hydrodynamic modeling proves that similar bipolar nebular structures can be obtained by shaping an intermittent wind by an oblique shock against a stable circumbinary dust disk. On the other hand, the blue, purely scattered, light gives a spherical nebula except at its resolved center. Therefore, the outstanding problem in explaining the morphology of the RR is still the exact reconstruction of the history of the different structural components. It is also possible that the variety of geometric elements in the RR nebula arises from the remarkably large ratio of thickness of the circumbinary dust disk to the orbital dimensions, which greatly enhances the possibilities for continued interaction between the bipolar flows and the circumstellar environment.

7. Acknowledgments

MC and HEB thank STScI for support through grant HST-GO-07297.

REFERENCES

Artymowicz, P., Clarke, C. J., Lubow, S. H., & Pringle, J. E. 1991,

Aitken, R. G. 1918, Lick Obs. Bull., 9, 133

Bond H.E., Fullton L.K., Schaefer K. et al., 1997, in IAU Symp. 180, “Planetary Nebulae”, 211

Bujarrabal, V., Neri, R., Alcolea, J., & Kahane, C. 2003, preprint

Cernicharo, J., Heras, A.M., Tielens A.G.G.M., et al. 2001, ApJ, 546, L123

Cohen, M., Anderson C.M., Cowley A., et al. 1975, ApJ196, 179

Cox, P., Lucas, R., Huggins, P.J., et al. 2000, A&A 353, L25

Glinski, R.J., Lauroesch, J.T., Reese, M.D., Sitko, M.L., 1997, ApJ, 490, 826

Gull, T.R., Cohen, M., & Van Winckel, H. 2003, in preparation

Heintz, W. D. 1980, ApJS, 44, 111

Holden, F. 1975, PASP, 87, 945

Icke, V. 1981, ApJ, 247, 152

Icke, V., 2002, in IAU Symp 209, “Planetary Nebulae: their Evolution and Role in the Universe”, in press.

Jura, M., Turner, J., & Balm, S.P. ApJ474, 741

Jura, M., Turner J.L., Van Dyk, S., & Knapp, G.R. 2000, ApJ528, L105

Kwok, S., Hrivnak B.J., & Su, K.Y.L. 2000, ApJ544, L149

Meaburn, J., Walsh, J. R., Hebden, J. C., Morgan, B. L., & Vine, H. 1983, MNRAS, 205, 53P

Men'shckikov, A.B., Schertl, D., Tuthill P.G., Weigelt, G., & Yungelson, L.R. 2002, A&A, 393, 867

Miyata, T., Kataza, H., Okamoto, Y. K., Onaka, T., Sakao, S., Honda, M., Yamashita, T. & Murakawa, K. 2003, A&A, submitted

Osterbart R., Langer N., Weigelt G. 1997, A&A325, 609

Price, S. D. & Walker, R. G. 1976, "The AFGL four color infrared sky survey: Catalog of observations at 4.2, 11.0, 19.8, and 27.4 micrometers", Environmental Research Papers (Hanscom AFB, MA), AFGL-TR-0208

Roddier F., Roddier C., Graves J.E., Northcott M.J., 1995, ApJ443, 249

Sarre P.J., Miles J.R., Scarrott S.M., 1995, Science 269, 674

Sahai, R., Trauger, J.T., Watson A.M., et al. 1998, ApJ493, 301

Sahai, R., Hines D.C., Kastner J.H., et al. 1999, ApJ, 492,L163

Sahai, R., Zijlstra, A., Bujarrabal, V., te Likkel Hekkert, P., 1999, AJ 117, 1408

Sahai, R., te Lintel Hekkert, P., Morris, M., Zijlstra, A., Likkel L., 1999, 514, L115

Sahai, R., Bujarrabal V., Zijlstra, A., 1999, ApJ 518, L115

Scarrott S.M., Watkin S., Miles J.R., Sarre P.J., 1992, MNRAS, 255, 11

Schmidt G.D., Cohen M., Margon B., 1980, ApJ, 23, L133

Simis, Y., Icke, V., Dominik, C., 2001, A&A, 371, 205

Soker, N. 2002, ApJ, 570, 369

Ueta, T., Meixner M., Bobrowsky M., 2000, ApJ, 528, 861

Van Winckel H., Waelkens C., Waters L.B.F.M., 1995, A&A293, L25

Van Winckel H., Cohen M., Gull T.R., A&A, 390, 147

Waelkens, C., Van Winckel, H., Waters, L.B.F.M., Bakker, E.J. 1996, A&A314, L17

Waters, L.B.F.M., Waelkens C., Van Winckel, H., et al., 1998, Nature391, 868

Weaver, H.F. 1974, Highlights of Astronomy, 3, 509 (IAU)

Witt A.N., Boroson T.A., 1990, ApJ355 , 182

This preprint was prepared with the AAS LaTeX macros v5.0.

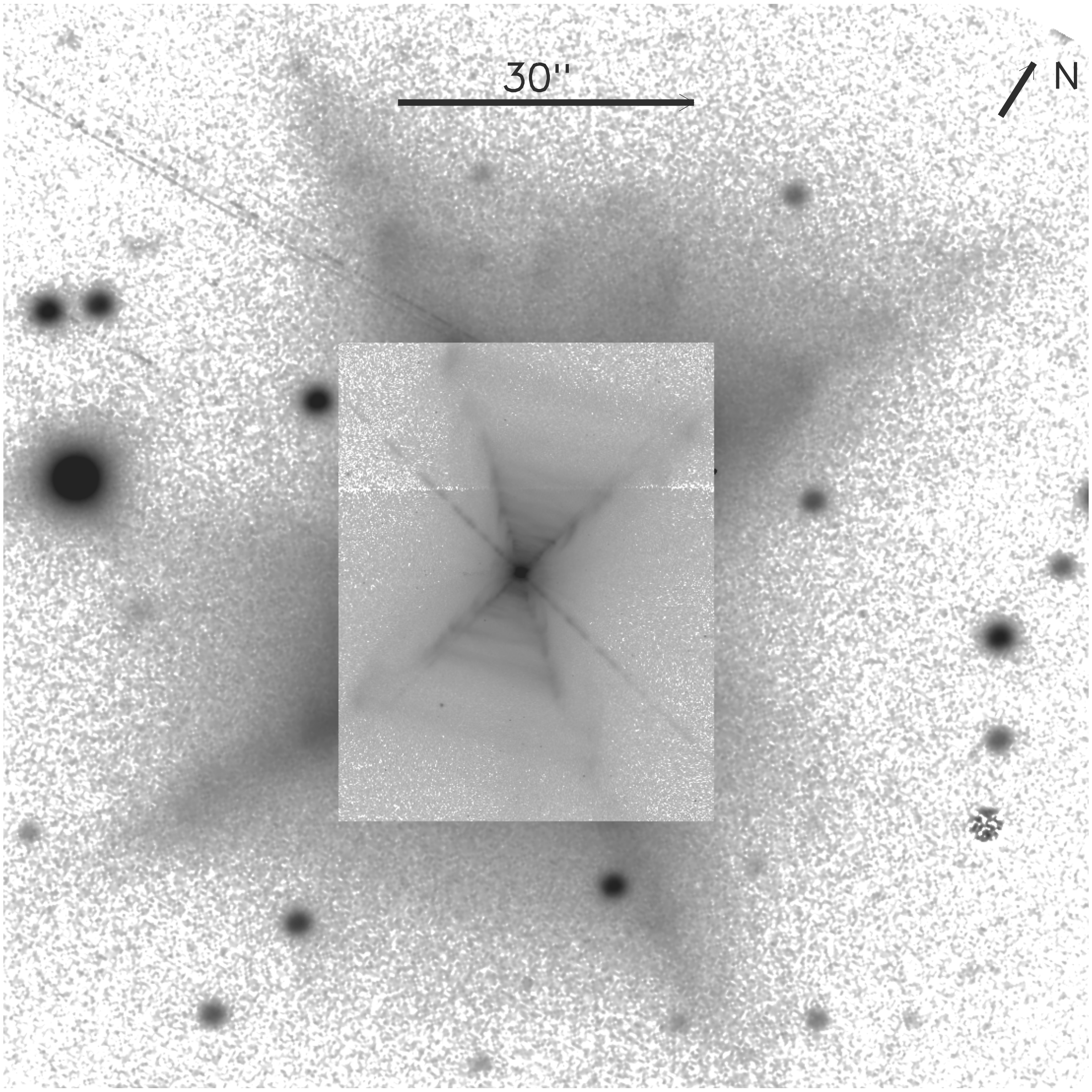

Fig. 1.— Ground-based ESO NTT Hα coronographic image, with the scaled *HST* F588N WFPC2 image superposed on the central region. The curious object near the lower right corner of this image is an artifact caused by the use of our simple coronograph: a glass plate with different sized black dots. While the biggest dot obscured the center of HD 44179, another dot obscured the region of the sky in which this artifact appears after reduction in the final image.

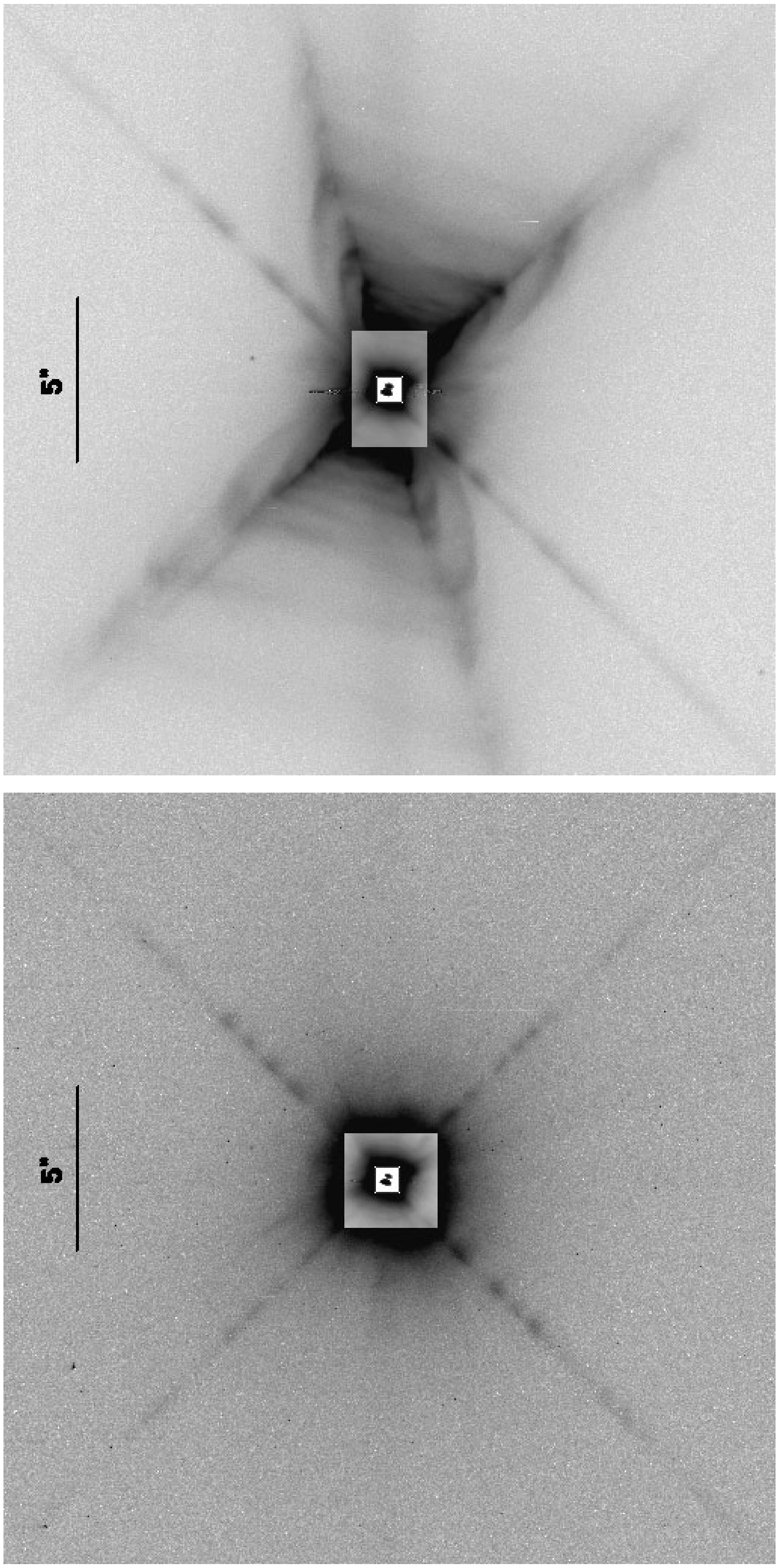

Fig. 2.— Left: F467M PC-image; right panel: *HST* WFPC2 F622W PC-image. Note the resolved center and the strikingly different appearance of the nebula due to the ERE contribution in the F622W filter. Insets show different intensity cuts. The inner region is resolved with a dark optically-thick dust lane at the center. North is to the lower right (120° clockwise from vertical), and east is to the upper right (30° clockwise from vertical).

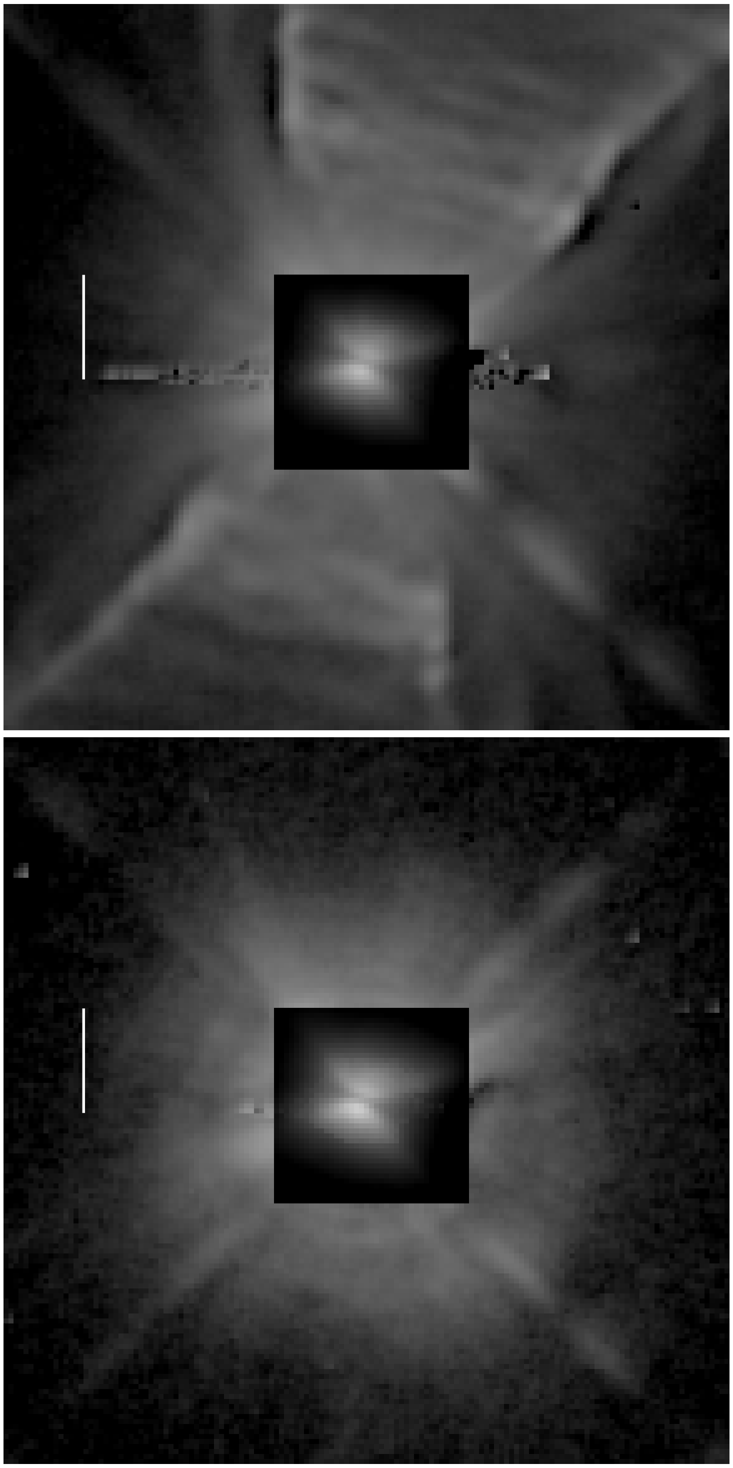

Fig. 3.— Left: the central part of the F467M PC-image. Right: the combined F631N, F622W, F588N PC-image, slighly sharpened. Note the resolved center and the strikingly different appearance of the nebula due to the ERE's contribution in the red. Insets show different intensity cuts of the unsharpened images. The inner region is resolved with a dark, optically-thick, dust lane in the center of the nebula. The blue reflection nebula is strikingly spherical with hints of concentric arcs but detailed analysis shows these are PSF-related. White bars show $1''$. North is to the lower right (120° clockwise from vertical), and east is to the upper right (30° clockwise from vertical).

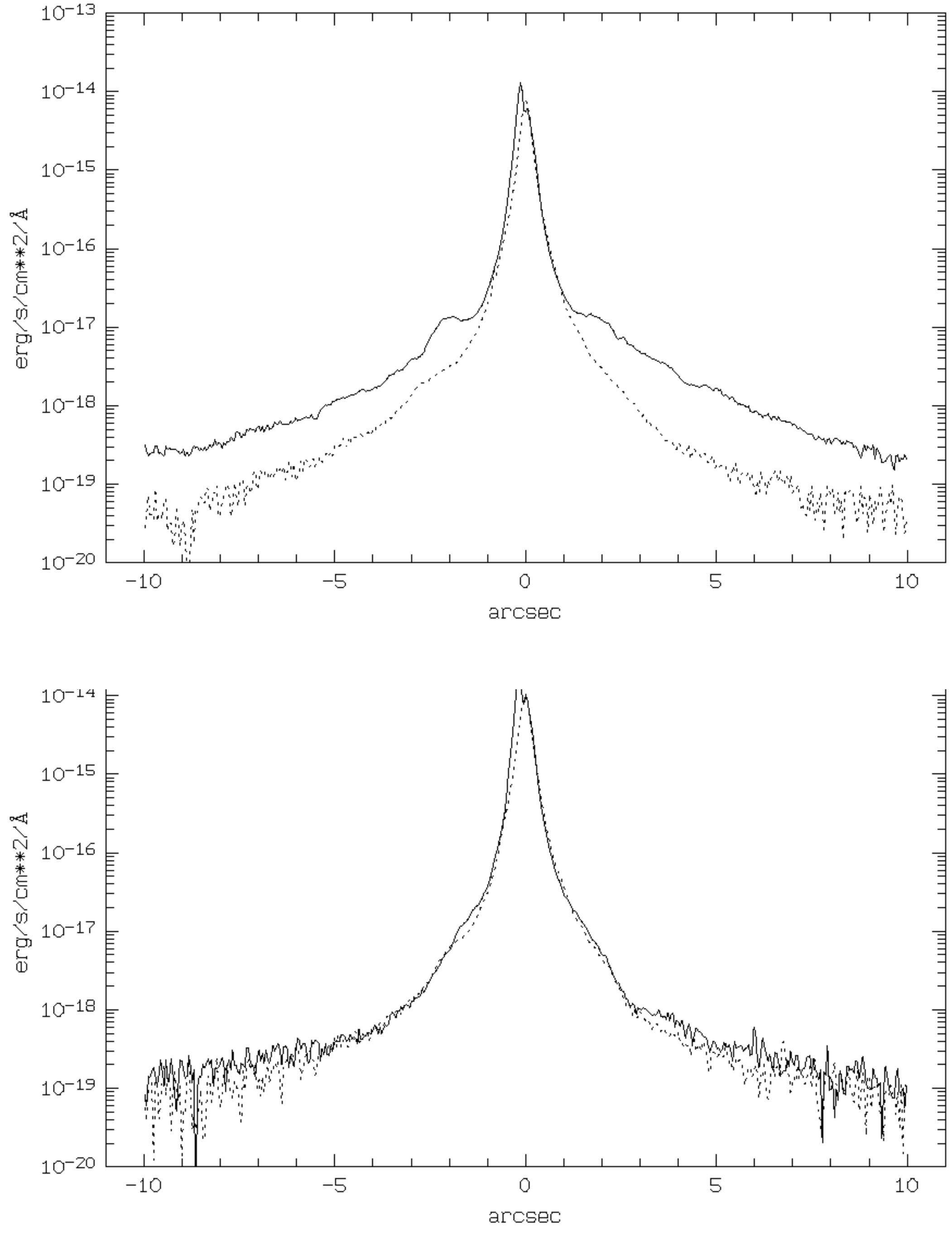

Fig. 4.— Flux density traces of the F467M PC-image (bottom) and the F622W PC image (top). The solid line is a trace along the polar symmetry axis of the nebula, while the dotted line shows the orthogonal trace. Except for the resolved center, in the blue the traces are very similar. This is clearly not the case in the ERE-dominated F622W red filter.

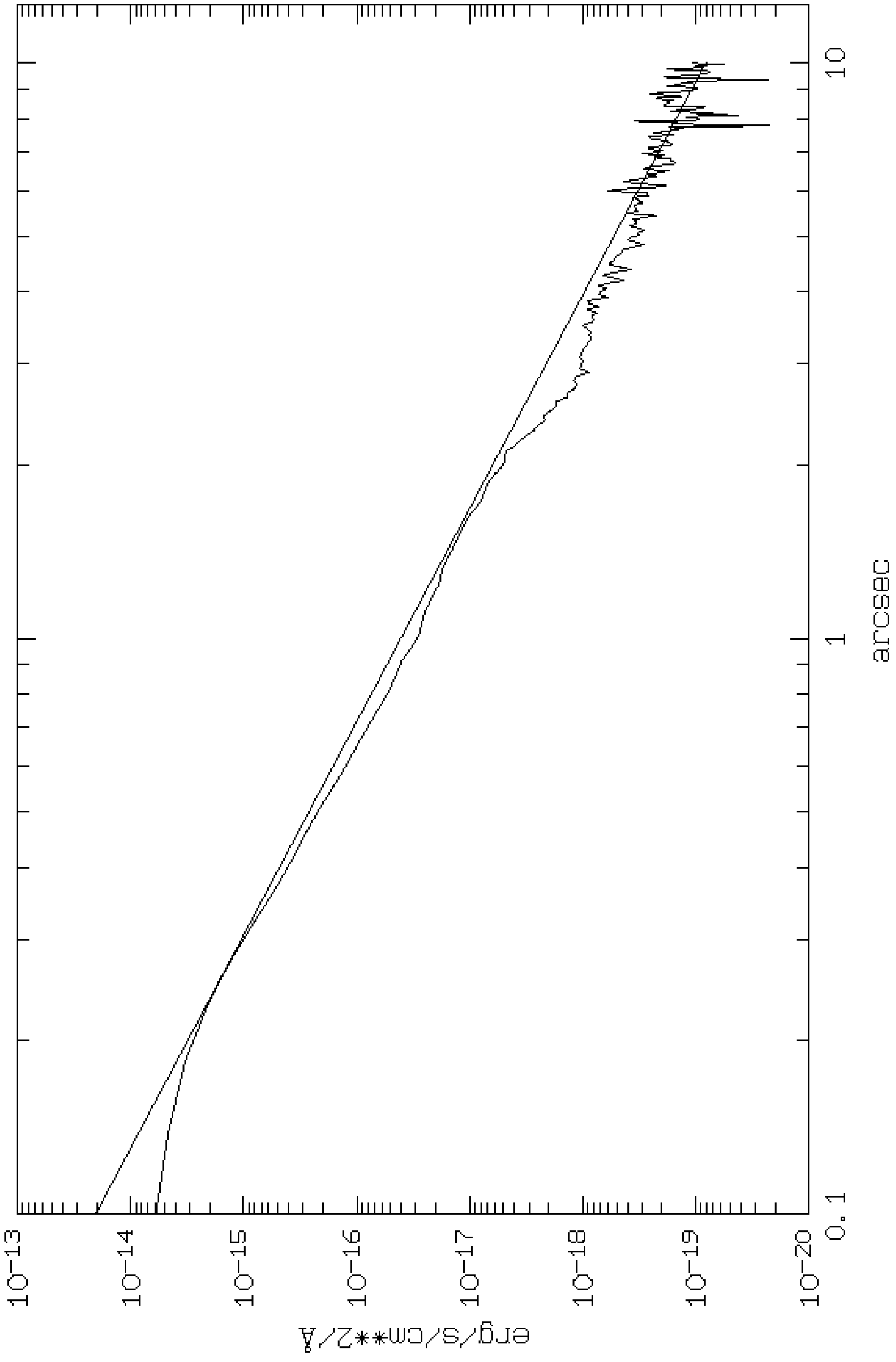

Fig. 5.— The intensity spatial profile of the blue F467M filter is well represented by a power law $r^{-2.7}$.

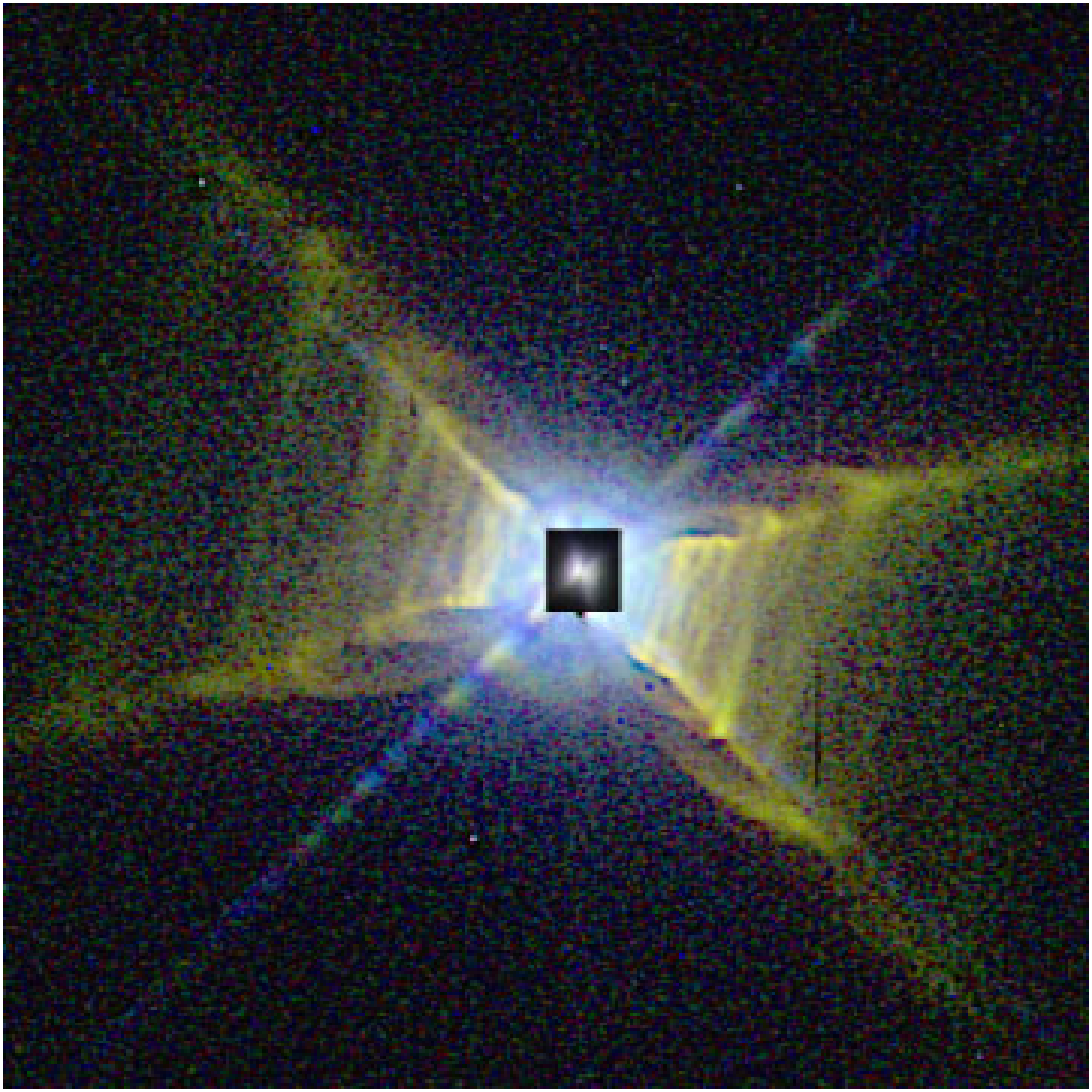

Fig. 6.— Three-color "rgb" PC image in PC F631N (R), F588N (G), and F467M (B) showing the confinement of blue scattered starlight to the inner central parts of the RR. Individual images of the color composite were extracted and the logarithms of the sharpened images were byte-scaled and combined. The inner portion was byte-scaled differently and is unsharpened. The apparent blue ring, concentric with the scattered light component nea the center of RR, is a PSF-related artifact. Total dimensions of the figure are $23.3'' \times 23.3''$. North is to the lower right (120° clockwise from vertical), and east is to the upper right (30° clockwise from vertical).

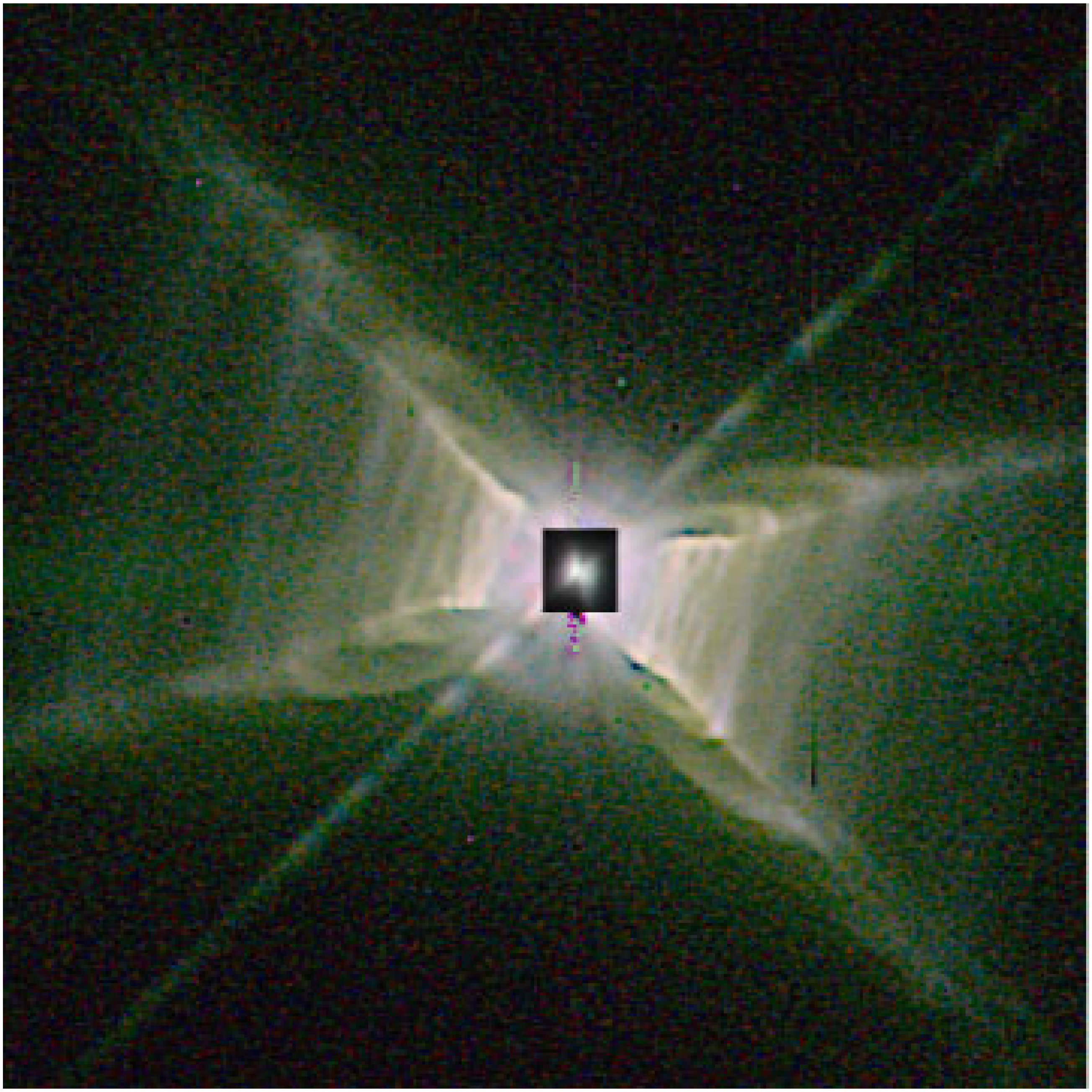

Fig. 7.— Three-color “rgb” PC image in PC F631N (R), F622W (G), and F588N (B), showing the almost total absence of color, implying that all structures have virtually identical appearances in these three filters. Each of the RGB images was individually sharpened and logarithm versions were byte-scaled and combined. The inner portion was byte-scaled differently and is unsharpened. Total dimensions of the figure are $23.3'' \times 23.3''$. North is to the lower right (120° clockwise from vertical), and east is to the upper right (30° clockwise from vertical).

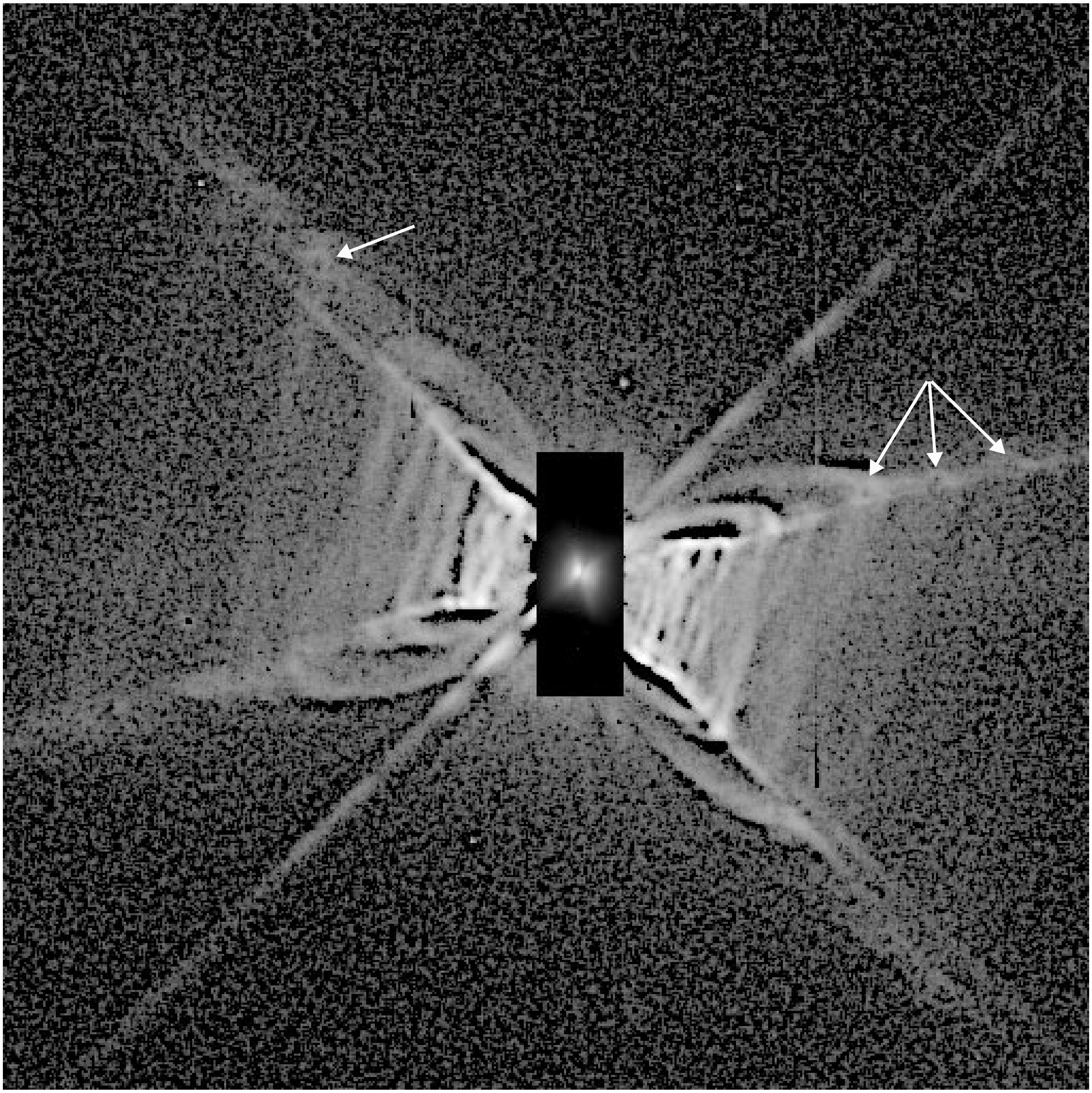

Fig. 8.— Unsharp-masked 9×9 PC image using the inverse-variance weighted average of the three identically masked images in F631N, F622W, and F588N. The arrows indicate the location of the most apparent vortices. The inset is from the original, unsharpened image. North is to the lower right (120° clockwise from vertical), and east is to the upper right (30° clockwise from vertical).

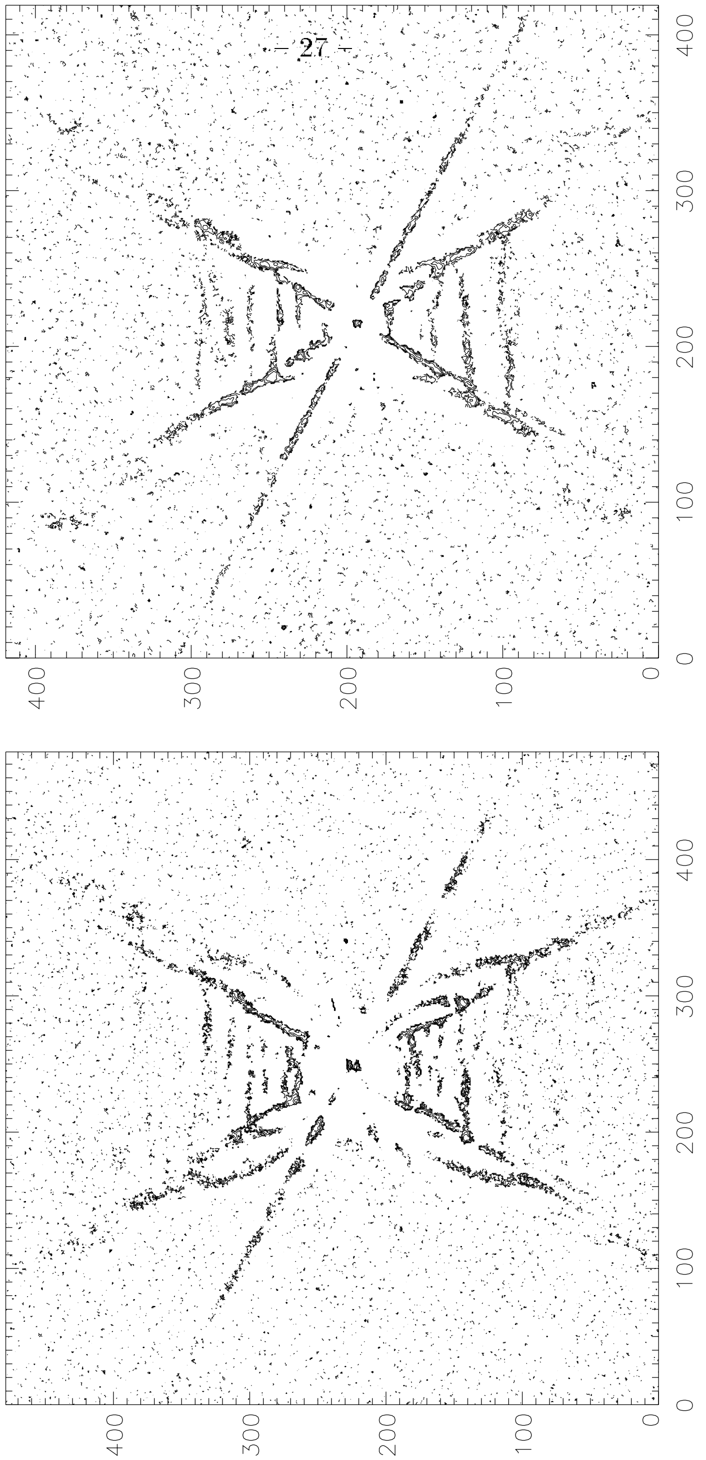

Fig. 9.— Left: Contour plot of the 9×9 sharpened combined images of the PC (the weighted sum of F631N, F622W, F588N images). The total size shown is $21.9'' \times 21.9''$, corresponding to a 480×480 pixel subimage of the original 800×800 PC image. Right: Contour plot of the 9×9 sharpened combined images of the WF (F631N, F588N). The total size shown is $41.8'' \times 41.8''$, corresponding to a 420×420 pixel subimage of the original 800×800 WF image. In both images, north is up and east to the left.

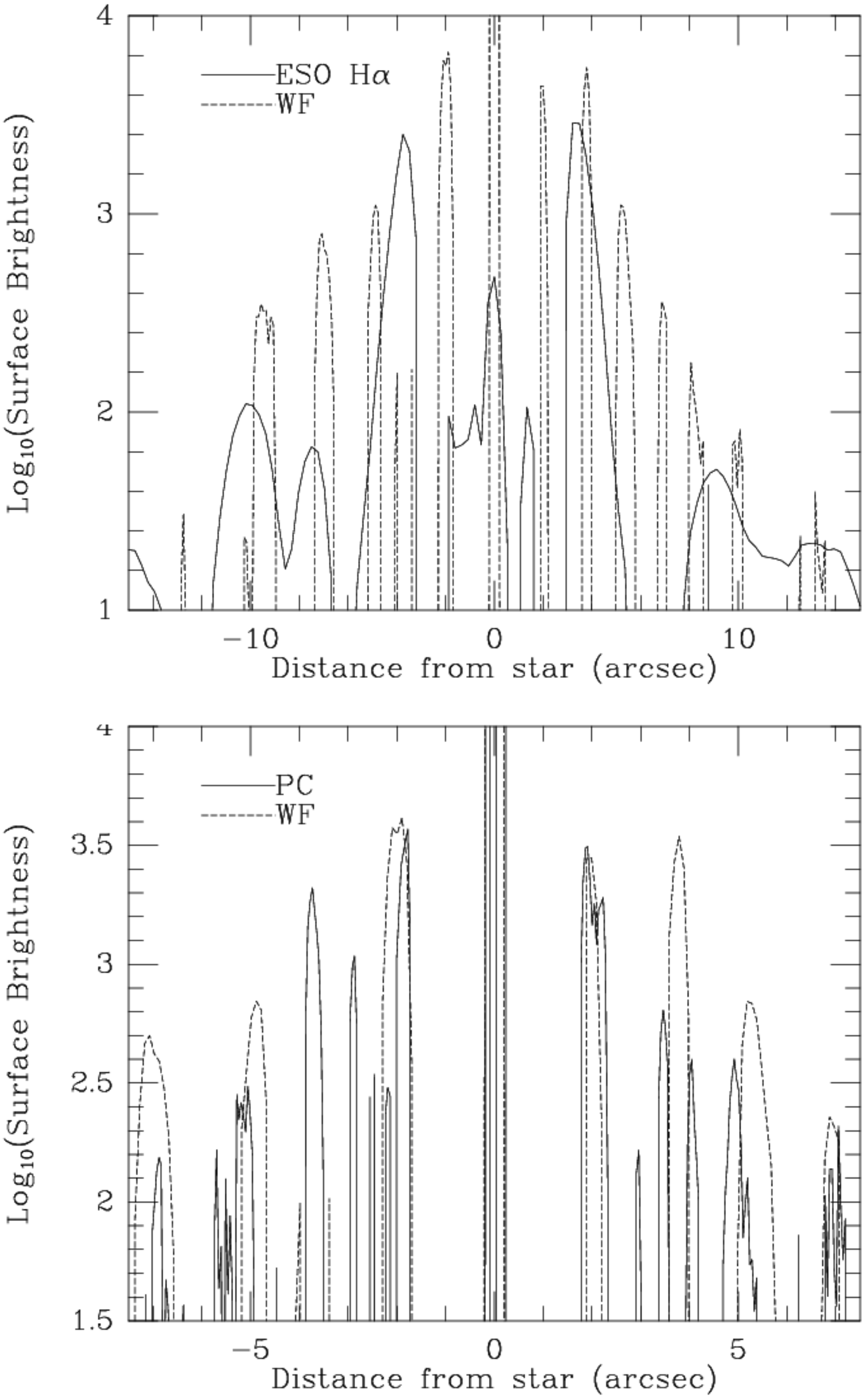

Fig. 10.— Bottom: The innermost spatial surface brightness profile along the RR's axis of symmetry, measured from the WF mosaic and in the PC1 chip. Top: Idem but from the ground-based ESO coronographic Hα image and the WF mosaic at intermediate distances from HD 44179.

Table 1. Journal of ESO ground-based direct imaging observations

Date	Filter wavelength	FWHM	Exposure (s)	Comment
1998 Jan 26	ESO 6026Å	538Å	300	red continuum
1998 Jan 26	ESO 5028Å	266Å	1800	continuum
1998 Jan 25	ESO 6568Å	73Å	1200	H_α

Table 2. Journal of WFPC2 observations

Date	Rootname	Camera	Filter	Exposure (s)
1999 Mar 17	U50C0101R	PC1	F622W	0.7
1999 Mar 17	U50C0102R	PC1	F622W	40
1999 Mar 17	U50C0103R	PC1	F622W	40
1999 Mar 17	U50C0104R	PC1	F502N	40
1999 Mar 17	U50C0105R	PC1	F467M	260
1999 Mar 17	U50C0106R	PC1	F467M	260
1999 Mar 17	U50C0107R	PC1	F588N	14
1999 Mar 17	U50C0108R	PC1	F588N	160
1999 Mar 17	U50C0109R	PC1	F588N	160
1999 Mar 17	U50C010AR	PC1	F631N	26
1999 Mar 17	U50C010BR	PC1	F631N	160
1999 Mar 17	U50C010CR	PC1	F631N	160
1999 Mar 17	U50C010DR	WF3	F588N	500
1999 Mar 17	U50C010ER	WF3	F588N	500
1999 Mar 18	U50C010FR	WF3	F631N	500
1999 Mar 18	U50C010GR	WF3	F631N	500

Table 3. Principal mass loss events as represented by centroids of bright strands across the bicone. Columns parallel to the long axis of the bicone have been coadded. North and south peaks are paired whenever possible. Positive distances from HD 44179 are in the north lobe; negative distances in the south

Image	Distance(N) (arcsec)	Distance(S) (arcsec)	Confirmed	Comments
PC	+1.91	-1.83	WF +1.99,-1.98	N/S figure-8 strands with +2.18,-2.16
PC	+2.18	-2.16	WF +1.99,-1.98	N/S figure-8 strands with +1.91,-1.83
PC	· · ·	-2.51		
PC	+2.94	-2.88		S bifurcates; N/S partial figure-8 strands
PC	+3.47	-3.71	N: WF +3.76	S figure-8 strand, N with +4.05
PC	+4.05	· · ·		N figure-8 strand with +3.47
PC	+4.92	-5.14	WF +5.23,-4.95	N/S point-symmetric curved strands; N/S figure-8 strands?
PC	5.3	-5.50		
PC	· · ·	-5.68		
PC	+6.99	-6.90	WF +6.91,-7.02	S: inclined to bicone axis; figure-8 strands? not connected to bicone
WF	+8.20	-8.45		S: bifurcates to -8.45/-9.45; figure-8 strands?
WF	+10.03	-9.45	N: PC +9.17,+9.69, · · · S: ESO Hα -10.0	very faint, broad
WF	+14.00	-19.0	N: ESO Hα +13.6	
ESO Hα	+19.8	-23.9		
ESO Hα	+29.2	-33.5		
ESO Hα	+36.2	· · ·		
ESO Hα	+43.0	· · ·		

Table 4. Principal mass loss events as represented by a surface brightness profile along the NE-SW bicone edge. Columns parallel to and adjacent to this nebular spike have been coadded. NE and SW peaks are paired whenever possible. Positive distances from HD 44179 are in the NE lobe; negative distances in the SW

Image	Distance(NE) (arcsec)	Distance(SW) (arcsec)	Confirmed	Comments
PC	+2.13	-2.17	WF +2.09,-2.30	
PC	+2.83	-3.24	WF +3.17,-3.72	
PC	+3.63	···		
PC	+4.51	-4.30	WF +4.18,-4.62	
PC	···	-5.15		
PC	+5.96	-6.18	WF 6.36,-6.17	
PC	+7.03	-7.20	WF +7.22,-7.15	
PC	+7.93	-8.16	WF +8.05,-8.26	
PC	+9.41	-8.78	WF +9.56, -8.58	
PC	+10.14	-10.46	WF +10.22,-10.14	
WF	+12.44	-11.35		both broad
WF	+13.56	-12.96		